



HAL
open science

Deformation of an experimental drainage network in oblique collision

L. Guerit, Stephane Dominguez, Jacques Malavieille, S. Castelltort

► **To cite this version:**

L. Guerit, Stephane Dominguez, Jacques Malavieille, S. Castelltort. Deformation of an experimental drainage network in oblique collision. *Tectonophysics*, 2016, 693, Part B, pp.210-222. 10.1016/j.tecto.2016.04.016 . hal-01467564

HAL Id: hal-01467564

<https://hal.science/hal-01467564>

Submitted on 10 Nov 2020

HAL is a multi-disciplinary open access archive for the deposit and dissemination of scientific research documents, whether they are published or not. The documents may come from teaching and research institutions in France or abroad, or from public or private research centers.

L'archive ouverte pluridisciplinaire **HAL**, est destinée au dépôt et à la diffusion de documents scientifiques de niveau recherche, publiés ou non, émanant des établissements d'enseignement et de recherche français ou étrangers, des laboratoires publics ou privés.

Deformation of an experimental drainage network in oblique collision

L. Guerit^{a,*}, S. Dominguez^b, J. Malavieille^b, S. Castelltort^a

^a*University of Geneva, Department of Earth Sciences, Rue des Maraichers 13, 1205 Geneva, Switzerland*

^b*Université de Montpellier, Géosciences Montpellier UMR 5243, F-34095 Montpellier, France*

Abstract

In oblique collision settings, parallel and perpendicular components of the relative plate motion can be partitioned into different structures of deformation and may be localized close to the plate boundary, or distributed on a wider region. In the Southern Alps of New Zealand, it has been proposed that one-third of the regional convergence is distributed in a broad area along the Southern Alps orogenic wedge. To better document and understand the regional dynamics of such systems, reliable markers of the horizontal tectonic motion over geological time scales are needed. River networks are able to record a large amount of distributed strain and they can thus be used to reconstruct the mode and rate of distribution away from major active structures. To explore the controls on river resilience to deformation, we develop an experimental model to investigate river pattern evolution over a doubly-vergent orogenic wedge growing in a context of oblique convergence. We use a rainfall system to activate erosion, sediment transport and river development on the model surface. At the end of the experiment, the drainage network is statistically rotated clockwise, confirming that rivers can record the distribution of motion along the wedge. Image analysis of channel time-space evolution shows how the fault-parallel and fault-perpendicular components of motion decrease toward the fault and impose rotation to the main trunk valleys. However, rivers do not record the whole imposed rotation rate, which suggest that the natural lateral channel dynamics can alter the capacity of rivers to act as passive markers of deformation.

1. Introduction

Fault-offset rivers have been widely used as passive markers to quantify horizontal tectonic motions displacements on large-scale intracontinental strike-slip faults (Allen, 1965; Replumaz et al., 2001; Walker and Jackson, 2002; Hubert-Ferrari et al., 2002; Hollingsworth et al., 2008; Hubert-Ferrari et al., 2009; Klinger et al., 2011; Li et al., 2012). However, the use of active rivers and river networks to quantify the amount of deformation distributed away from localized tectonic structures is not straightforward. In fact, active geomorphic processes such as lateral erosion and river captures (Bishop, 1995; Brookfield, 1998; Hallet and Molnar, 2001; Clark et al., 2004) demonstrate clearly that drainage networks are dynamic entities organizing and reorganizing themselves

*Corresponding author

8 when submitted to external forcings such as tectonic deformation (Brocard et al., 2003; Clark et al., 2004; Brocard et al., 2012;
9 Babault et al., 2012; Willett et al., 2014; Lavé, 2015; Ferrater et al., 2015) and climate change (Tucker and Slingerland, 1997; Roe
10 et al., 2003; Bonnet, 2009; Attal, 2009; Giachetta et al., 2014; Yang et al., 2016). Recently, several studies have proposed that
11 river networks may in some cases act as faithful markers of large-scale surface horizontal displacements. Hallet and Molnar (2001)
12 document for instance the distortion of several major rivers in the eastern Himalayan syntaxis in response to the indentation of
13 India into Asia, thus suggesting that these rivers have acted as passive markers of the large scale distributed deformation in this
14 area. Similarly, Ramsey et al. (2007) in Taiwan and Castelltort et al. (2012) in the Southern Alps of New Zealand (Figure 1)
15 observe that rivers draining the orogen are deviated in a systematic pattern from the normal perpendicular drainage orientation
16 classically observed in linear mountain ranges (Hovius, 1996; Castelltort and Simpson, 2006; Perron et al., 2008). Castelltort
17 et al. (2012) propose that this orientation results from progressive shearing of initially transverse rivers that are thus suggested to
18 act as passive markers of the deformation field. Yet, these authors remark that interfluves and a significant area of the drainage
19 network of the Southern Alps encompass some degree of river capture and reorganization. Such dynamic behavior of drainage
20 networks in response to tectonic deformation is illustrated by Yang et al. (2015). These authors used the χ metric and numerical
21 experiments to demonstrate that the drainage pattern studied by Hallet and Molnar (2001) has been disrupted to some extent,
22 leaving the major streams actively incising in the landscape and acting like passive markers of deformation, while interfluves are
23 left as isolated remnants starved of drainage area, unable to balance tectonic uplift. Recently, Goren et al. (2015) document
24 another example of large-scale distributed crustal deformation that is recorded in the arrangement of transverse rivers draining
25 Mount Lebanon.

26 The fundamental problem outlined by these studies is the extent to which a drainage network is able to deform under a given
27 tectonic strain field, and to retain a record of that deformation until it yields and loses memory (Kirby, 2012). This problem
28 is crucial because it determines our ability to use river patterns to understand the partitioning of deformation at the Earth's
29 surface between narrow zones of localized deformation and broad areas of distributed strain (Molnar et al., 1999; Hallet and
30 Molnar, 2001; Ramsey et al., 2007; Castelltort et al., 2012). To complement the field observations and the numerical approaches
31 undertaken in the studies cited above, we developed laboratory geomorphic experiments including tectonic and surface processes
32 (erosion, sedimentation) couplings to describe and understand the response of a drainage network to a large scale horizontal
33 deformation. We chose an oblique collisional context in which deformation is expected to be partitioned (Braun and Beaumont,
34 1995; Burbidge and Braun, 1998; Martinez et al., 2002; Upton et al., 2003; Leever et al., 2011) and that can be discussed with
35 reference to the deformed drainage network of the Southern Alps of New Zealand. This paper documents the development of

36 the experimental orogenic wedge, with a particular focus on the deformation of the drainage network on its surface.

37 **2. Experimental approach**

38 *2.1. General boundary conditions inspired by the Southern Alps of New Zealand*

39 Our objective is to perform analogue experiments in oblique setting with strain partitioning as observed in the Southern
40 Alps of New Zealand, in order to study the plausibility of river deformation in such context. Therefore, the experimental model
41 geometry, rheology and kinematic boundary conditions were inspired by the Southern Alps of New Zealand, but the regional
42 specificities of the range are not considered.

43 Orogenic wedge morphology corresponds to an asymmetric doubly-vergent wedge, with a short and steep retroside and a longer
44 proside with a lower slope (Figure 2a) (Willett et al., 1993; Koons, 1994). The Alpine Fault, separating the upper Australian
45 plate to the North-West from the lower Pacific plate to the South-East, is the main tectonic structure of the range (Figure 1a).
46 This major oblique strike-slip fault has accommodated about 400 km of lateral offset since the Cenozoic, and slip presently at
47 about 40 mm/y with a convergence angle of 11 ° (Molnar et al., 1999; Wallace et al., 2007; Cox and Sutherland, 2007; Castelltort
48 et al., 2012; Norris and Toy, 2014). The strike-parallel motion is of 35-40 mm/y and the strike-perpendicular component amounts
49 to 7-8 mm/y (Walcott, 1998; Sutherland, 1999; Castelltort et al., 2012; Norris and Toy, 2014). Several observations suggest that
50 the current relative plate motion is not entirely accommodated by slip along the Alpine Fault. Molnar et al. (1999) first pointed
51 out the discrepancy between paleogeography reconstructions and the actual offset of remarkable terranes, which suggests that
52 part of the total strain has been distributed away from the main plate boundary. In addition, Norris and Cooper (2001) showed
53 that the offsets of quaternary geomorphic markers on the Alpine Fault do not match with the expected offsets deduced from the
54 current plate motion. Finally, Castelltort et al. (2012) showed that the large-scale long-term and short-term discrepancies are
55 compatible with the deformation of transverse rivers on the Eastern flank of the range. These studies suggest that only two-third
56 of the motion is actually localized on the Alpine Fault itself while the remaining motion is distributed across the Southern Alps
57 (Norris and Cooper, 2001; Castelltort et al., 2012; Norris and Toy, 2014).

58 At crustal scale, the range consists of a 15-km-thick layer of greywackes overlying about 15 km of schists (Figure 2a)(Cox and
59 Sutherland, 2007; Herman et al., 2009). These materials, in particular the top layer of sandstones and greywackes, are affected
60 by reverse faults that accommodate the deformation with an oblique displacement (Cox and Sutherland, 2007; Herman et al.,
61 2009; Norris and Toy, 2014). Except for the Alpine Fault, these structures appear limited in width and rarely exceed 25-30 km
62 in length (Norris and Toy, 2014, and references herein).

63 The present-day rainfall over the Southern Alps is strongly affected by the rain-shadow effect which stops the precipitations
64 brought by the Westerlies. Rainfall decreases from ~ 12 m/y on the west side of the range to less than 1 m/y on the east side
65 (Griffiths and McSaveney, 1983). This asymmetric rainfall pattern is believed to influence the general exhumation pattern of the
66 range as erosion rates correlate strongly with the precipitations, being maximal on the west flank (Adams, 1980; Hicks et al.,
67 1996; Cox and Sutherland, 2007).

68 *2.2. Setup and experimental run*

69 The experiment presented in this paper was performed in the Géosciences Montpellier laboratory. We used a table of 2.6
70 x 1.4 m covered by a carbon-kevlar film pulled by a computerized stepping motor on one side of the table (Graveleau et al.,
71 2015). The motion of the film, which corresponds to the shortening rate of the experiment, is set to 7.5 cm/h. A rigid aluminum
72 frame positioned at $\sim 30^\circ$ with respect to the motion direction and with a dip angle of 60° imposes a velocity discontinuity that
73 controls the development of the wedge (Figure 2b and 2c). The analogue material is loaded on the film, moved toward the
74 oblique backstop and undergoes compression. The maximum shortening is limited by the size and the geometry of the setup, i.e.,
75 ~ 80 cm in the present configuration. A doubly-vergent accretionary wedge develops in-sequence by the progressive propagation
76 of frontal thrusts. Due to the cross-sectional geometry, with a horizontal basal décollement and a steep backstop, the wedge
77 develops asymmetrically with a long and gentle slope at the proside and a short and steep slope at the retroside (Willett et al.,
78 1993; Martinez et al., 2002) (Figure 2c). The main parameters and geometry of the experiment are summarized in Table 1.

79 Sprinklers above the deformation table generate rainfall in the form of micro-droplets of water. This rainfall system induces
80 water run-off on the model surface which produces erosion, sediment transport and deposition such that a drainage network
81 progressively develops on the sides of the wedge. Precipitations were made intermittent to enhance erosion over the model surface
82 (12 s wet for 8 s dry). In order to simulate the effect of the precipitation gradient observed between the western and eastern
83 sides of New Zealand (Griffiths and McSaveney, 1983), the sprinklers are placed such that mean rainfall rate decreases from 50
84 mm/h at the northern edge of the model to a few mm/h at its southern edge.

85 *2.3. Analogue materials*

86 To reproduce the first-order rheological layering of the Southern Alps crust (Cox and Sutherland, 2007; Herman et al., 2009),
87 we designed a two-layer model. We used a granular mix, the MatIV, to model the brittle behavior of the upper-crustal layer
88 and the evolution of surface morphology (see Graveleau et al., 2011, for the complete description of the MatIV properties). This
89 granular mix is composed of 46% of glass beads with a median diameter of 100 to 200 μm , 24% of PVC and 30% of silica powder
90 and was specifically developed to model the interactions between deformation, erosion and sedimentation (Graveleau et al., 2011,

91 2015). A few percent of graphite ($\sim 1\%$) is added to MatIV to improve syntectonic sediment bedding contrast and the accuracy
92 of model surface kinematics measurements (see the Measurements subsection). However, MatIV is brittle, it deforms by faults
93 and is therefore not suitable to simulate the behavior of the middle-lower crust, where deformation is neither purely brittle or
94 ductile. This lower layer must be less resistant mechanically than MatIV in order to propagate strain but it must also be able
95 to accommodate deformation by faults, and it must be erodible under the rainfall system when it reaches the surface along the
96 backstop, on the retorside of the experimental wedge. We thus developed a new analogue material named hereafter MTK based
97 on the MatIV composition, in which the silica powder is replaced by kaolinite and talcum, which presents a mechanical behavior
98 close to clay (Table 2). Water is then added to the powder to obtain a paste that can be spread evenly on the experimental
99 table. Water represents 20% of the final weight for MatIV and 25% for MTK (Table 2). MTK exhibits less brittle mechanical
100 behavior, as shown by its lower coefficient of internal friction (0.46) and cohesion (280 Pa) determined experimentally (Table 2,
101 Figure 3a) using the procedure of Graveleau et al. (2011). Yet, this material erodes in the shape of incised valleys with steep
102 hillslopes (Figure 3b).

103 The basal film is covered by a layer of glass beads to insure a low friction basal décollement simulating the intra-crustal
104 décollement that allows the growth of the Southern Alps wedge. This taper layer is 1-cm thick close to the backstop, and its
105 thickness decreases linearly to zero 60-cm further (not shown on Figure 2c). We then loaded the table with MTK to reach a
106 thickness of 3 cm all over the table. At this point, we added a thin layer of glass beads (~ 1 mm) to absorb the water seeping from
107 MTK to the surface, to prevent any mixing between the two materials. This layer will also help to visualize the discontinuity
108 between the materials in cross-sections. The upper layer is composed by 3 cm of MatIV. To better visualize deformation within
109 this material, we added more graphite to the first centimeter, which will appear darker while preserving the same mechanical
110 properties. The total thickness of the model is thus 6 cm, which corresponds to the backstop height (Figure 2c). The surface of
111 the model is flat at the beginning of the experiment.

112 *2.4. Measurements*

113 The evolution of the experiment is recorded by a 21 Mpx Canon 5D mark II camera located above the model. It covers a
114 field of view of 130 cm \times 70 cm with a resolution of 0.27 mm/pixel. Image acquisition is controlled by a computer and pictures
115 are taken every 30 seconds. We use ENVI and GMT to perform sub-pixel image correlation of these pictures using a correlation
116 window of 64 \times 32 pixels to determine the incremental horizontal velocity field at each time step (between two pictures) over the
117 whole wedge surface. The resulting velocity maps have an horizontal spatial resolution of 0.9 mm and an accuracy of about less
118 than 50 microns.

119 Laser interferometry is used to derive a digital elevation model (DEM) at different stages of model evolution (see Gravelleau
120 and Dominguez, 2008, for additional informations). During DEM acquisition, the model surface must be dry so the shortening and
121 rainfall are paused between 45 minutes and one hour to dry the very first millimeters of the model surface. The laser interferogram
122 is processed using SNAPHU software (Chen and Zebker, 2002) to unwrap the signal and obtain a regular topographic grid. The
123 resulting DEMs have similar horizontal and vertical resolution of about 0.5 mm. The duration of individual experiments is
124 limited to 3 days because beyond this duration the behaviour of the material and the stability of the laser measurements both
125 evolve. Given the maximum duration of experiments, the repeated 45-minutes pauses to acquire a full high-resolution DEM
126 every 5 cm of shortening, and the length of the experimental apparatus, the optimal shortening rate that we can perform is 7.5
127 cm/h. Accordingly, each picture corresponds to an increment of 0.6 mm of shortening. At the end of the experiment, the model
128 is left to dry for 3 to 4 days and then cut manually to obtain a 3D view of the internal structure of the wedge through serial
129 cross sections.

130 The average position of the wedge front was extracted automatically from the velocity maps. The front position is defined
131 as the position of the main velocity gradient and is then averaged over 2.5 mm of shortening (i.e., over four pictures). We use
132 RiverTools to extract the drainage network from the DEMs and MATLAB to calculate the average orientation of the rivers.
133 Main orientation corresponds to the weighted orthogonal least squares fit of a straight line to all the river pixels (Krystek and
134 Anton, 2011). In addition to this quantitative analysis, some channels were mapped on pictures and their mean orientation was
135 determined visually.

136 **3. Results**

137 In this section, we describe the evolution of the wedge and the drainage network during one experiment. These results were
138 successfully reproduced in a second experiment but are not presented hereafter for the sake of brevity.

139 *3.1. Evolution of the wedge and drainage patterns through time*

140 The evolution of the wedge is illustrated by a series of consecutive pictures (Figure 4a–h) and associated DEMs (Figure 5).
141 The main terms used to describe the wedge (divide, proside, retroside) and the spatial orientation of the model are shown on
142 Figure 4i. In all experiments, gravitational slidings and collapses took place on the retroside, disturbing the evolution of the
143 drainage pattern on this side of the orogen. To limit gravitational instability, future experiments shall be performed with larger
144 erosion rates on the retroside in order, and to date, this part of the model has been excluded from the analyses. On the prowedge

145 however, the lower slope inhibits gravitational processes and a large drainage network develops, similar to the one of the proside
146 (South-East) in the Southern Alps of New Zealand.

147 At the beginning of the experiment, the surface is flat. After 2.5 cm of shortening, a first thrust named T1 emerges ~ 10 cm
148 southward of the velocity discontinuity, i.e., of the position of the backstop at depth (S point). This fault is composed by long
149 segments (~ 9 cm) trending nearly perpendicular to the shortening direction and by short segments (~ 3 cm) running almost
150 parallel to the shortening direction. It marks the active front of the wedge up to about 20 cm of total shortening. During this
151 first stage, the wedge elevation increases and small streams start developing on its surface (Figures 4a, 4b, 5a and 5b). A second
152 thrust T2 then reaches the surface on the west side on the model (Figures 4c and 5c) before extending along the whole wedge
153 (Figures 4d and 5d). At this point, a network of transverse rivers seems to become permanent. After ~ 50 cm of shortening,
154 a third thrust T3 appears southward. At this stage, the prowedge is 25 cm in width on average (Figures 4e and 5e), rivers
155 lengthen and tend to flow toward the West (Figure 4f). After 20 cm of additional shortening (i.e., 70 cm of total shortening),
156 a fourth thrust T4 develops and marks the new active wedge front (Figures 4g and 5g). The prowedge is 40 cm in width and
157 the maximum elevation is 12 cm. During the 10 last cm of shortening, rivers continue to erode their banks, to transport and to
158 deposit sediments downslope (Figures 4h and 5h).

159 The width of the wedge is controlled by the emergence of these four successive thrusts at the front of the wedge. In
160 consequence, the average width tends to grow step by step, by the sudden addition of increments of ~ 10 cm in width (Figure
161 6). However, the position of the front is not fixed between two increments. On the contrary, it moves backwards toward the
162 orogen, as highlighted by the red arrows on Figure 6. We interpret this retreat as related to the accommodation of continuous
163 deformation such as folding on the hanging-wall, on the frontal thrust, and also to some underthrusting processes (Gutscher
164 et al., 1996; Santimano et al., 2015).

165 The cross-sections obtained at the end of the experiment are presented on Figure 7. The internal structure is equivalent
166 along each section and is typical of accretionary wedges (Davis et al., 1983). Remnants of the first thrust T1 are found in the
167 elevated part of the wedge close to the backstop (Figure 7). This thrust, which was probably continuous at first, is fragmented in
168 several small faults, with an average dip of 10° . A few centimeters toward the front, a more continuous fault is observed which
169 corresponds to the second main thrust T2. This fault can be split into two or three segments dipping at $25-30^\circ$. These two
170 structures are affected by numerous, but small, secondary reverse faults which accommodated part of the shortening. The third
171 thrust T3 dipping on average at 25° is generally continuous from the base of the wedge up to the surface. The position of this
172 fault is marked by the presence of well-preserved piggy-back basins. From these cross-sections, we can see that the last thrust

173 T4 is a major fault which affected the material over its entire thickness, down to the basal décollement. The dip of this fault
174 ranges between 20 and 30°. At the end of the experiment, the wedge thickness is close to twice the initial one in the thickest
175 part of the wedge (Figure 7).

176 Finally, it is important to note that the rivers developing on the surface of the wedge are highly dynamic (Figure 4). Drainage
177 basins are constantly evolving in response to fluvial erosion but also to the evolution of the topography. Sediments accumulate
178 at the front of the wedge in a large system of alluvial fans and these sedimentary systems are eventually advected into the range.
179 All along the experiment, rivers are abnormally oriented with their main flow direction primarily to the West (Figure 4). To
180 analyze and quantify this observation, we extracted the drainage network and calculated the average orientation of the main
181 rivers draining from the divide to the front of the wedge after ~80 cm of shortening (Figure 8). This reveals that, at the end of
182 the experiment, rivers are rotated clockwise by up to 35° (River 6).

183 *3.2. Horizontal velocity field across the wedge*

184 Sub-pixel image correlation measurements allows to obtain high-resolution velocity maps at the surface of the model. The
185 horizontal velocity field is determined between two consecutive pictures, thus every 0.6 mm of shortening throughout the run. As
186 an illustration, we here describe one example of the velocity field after 60 cm of shortening (Figure 9). The imposed shortening
187 rate is 7.5 cm/h, corresponding to 1.25 mm/min.

188 The velocity field outside the wedge is quite homogeneous in the yet undeformed areas, with a magnitude of 1.25 ± 0.06
189 mm/min and a mean orientation of $29.2 \pm 0.5^\circ$ with respect to the East-West (horizontal) axis of the figure. This is consistent
190 with the imposed convergence angle and velocity, and the observed variations might result from the experimental conditions and
191 analytical limitations. In our specific experimental setup, orientation and velocity are thus defined within a range of 5% and 10%,
192 respectively. The velocity abruptly changes after crossing the main frontal thrust. In fact, the amplitude of the velocity vector
193 evolves from 1.2 mm/min with orientation of 8 to 10° with respect to the EW axis, to less than 0.8 mm/min with orientation
194 of 6° at the backthrust fault (Figure 9). Northward of the main retro-fault, the velocity field falls to zero, as this area of the
195 experiment is fixed.

196 The velocity component parallel to the main fault, i.e., to the velocity discontinuity along the backstop and named hereafter
197 the fault-parallel component of the velocity, shows a clear evolution from South to North (in the figure reference frame, Figure
198 10a). The velocity is quite homogeneous in the undeformed area and is of 1.1 ± 0.1 mm/min. This rate decreases northward
199 between the front of the wedge and the divide, and velocity is typically around 0.8-1.0 mm/min, except in the most recent part
200 of the wedge on the west side of the model, where high velocity is still observed. Finally, the velocity decreases from 0.6 to 0.8

201 mm/min between the divide and the main fault (i.e., across the retro-side of the wedge). A minor EW pattern can be observed
202 and it could be related to material collapse at the edges of the experiment. Accordingly, the velocity field is deviated toward
203 the East on this side. The velocity component perpendicular to the plate boundary, named hereafter the fault-perpendicular
204 component, exhibits the same general pattern (Figure 10b). The velocity is quite homogeneous in the undeformed area of the
205 model, with an average rate of 0.5 ± 0.1 mm/min. Going northward, it decreases to 0.4 down to 0.2 mm/min right after the
206 front of the wedge and experiences a second fall to almost zero right after the former front of the wedge. Here again, we observe
207 slightly higher velocity on the west side of the wedge, which corresponds to the most recent active part of the wedge. This
208 velocity pattern implies that the horizontal compression is concentrated in the most frontal part of the wedge.

209 To summarize, the velocity observed at the surface of the wedge is a first order controlled by the frontal and the back thrusts,
210 and it evolves strongly between the two structures. In addition, it seems to be partially structured by the main tectonic features.

211 *3.3. Deformation at the surface of the wedge*

212 The velocity field described in the previous section is a combination of pure shear and simple shear, resulting in a general
213 rotation of the model's surface. For each velocity map, i.e., at each time increment, velocity was averaged in the longitudinal
214 section in order to discuss the displacement imposed to the rivers as a function of time and distance to the backstop (Figure
215 11). Scatter between individual, short-term increments is quite large but they can be averaged over time to better describe the
216 imposed velocity (Figure 11). It evolves across the wedge and in time, and so does the deformation imposed to any marker. In
217 the following we only focus on the pro-wedge, where the main rivers develop.

218 The fault-parallel (EW) component of model surface displacements decreases from the front of the wedge to the divide, at any
219 time during the experiment (Figure 11a). At first order, this component corresponds to a gradual decrease from the wedge front
220 to about 10 cm southward of the S-point (Figure 11a). This point corresponds closely to the wedge divide, northward of which
221 the EW velocity is quite constant (around 0.8 mm/min). The amount of distributed motion does not really change during the
222 experiment as the velocity intensity changes from 1.1 ± 0.1 mm/min in the undeformed area (from the south edge of the model
223 up to the wedge front) down to 0.8 ± 0.1 mm/min close to the divide (Figure 11a). However, as the length of the pro-wedge
224 increases with time (Figures 6 and 11), the shear is distributed over an increasingly larger area. In consequence, the intensity of
225 the deformation imposed by the EW horizontal velocity decreases through time. The fault-perpendicular (NS) velocity pattern
226 is more complex as the convex shape suggested on Figure 10b is maintained during the whole experiment. Similar to the EW
227 component, the amount of motion is quite stable through time and it evolves from 0.6 ± 0.1 mm/min in the deformed areas down
228 to 0.2 ± 0.2 mm/min close to the divide, with a minimum of 0.1 mm/min (Figure 11b). Here again, as the wedge widens in

229 time, the fault-perpendicular shear is distributed over an increasingly larger area and the resulting deformation decreases as the
230 experiment goes on. In addition to this first order pattern, this component appears segmented into a few steps (Figure 11b) in
231 relation to the former frontal thrusts, now advected into the wedge. Finally, it appears that about 30% of the EW motion and
232 50% of the NS motion is distributed across the wedge.

233 The two components of the velocity field act together to deform any marker at the surface of the wedge. This deformation
234 depends 1) on the maturity of the system and 2) on the orientation of the initial marker, and based on the average velocity field,
235 it is possible to model the deformation of a passive marker within the wedge. A straight line, with a given initial orientation
236 with respect to the North, is virtually placed on the surface of the wedge and at each step, this line is moved according to the
237 displacement it experiences. It is then prolonged up to the front of the wedge, with the same initial orientation. Figures 12a,
238 12b and 12c present the example of a marker with different initial orientation (0° , 20° and 40° , respectively) that would live
239 for the whole experiment. The peculiar behavior of the retro-wedge (between 0 and ~ 10 cm) has a clear signature in the final
240 morphology of the marker, but focusing on the pro-side only (i.e., from ~ 10 cm southward of the backstop to the wedge front),
241 the marker exhibits a general convex shape. However, working on a limited fraction of the marker, it is possible to define linear
242 segments, and thus, a principal orientation. Deformation can thus be modeled for any initial angle, for any initiation time and
243 for any duration, providing a framework to discuss the deformation pattern of the experimental drainage network.

244 4. Discussion

245 4.1. Influence of the experimental conditions

246 Classical analogue modelling approaches dedicated to the study of accretionary wedge evolution in oblique convergence setting
247 have been already performed using dry sand (e.g., Malavieille, 1984; Burbidge and Braun, 1998; Dominguez et al., 1998; Martinez
248 et al., 2002; McClay et al., 2004; Leever et al., 2011). In Martinez et al. (2002) and McClay et al. (2004), convergence angle
249 and total shortening were comparable to those used in our experiment but the impact of erosion on the wedge dynamics was
250 not taken into account. Our study provides, then, the first physical experiments of oblique convergence in a rainfall facility
251 including realistic erosion and material transfer processes. As typically observed in such a tectonic context, model morphology
252 and structure evolve into an asymmetric doubly-vergent wedge. The axial zone of this wedge is associated with short (few
253 centimeters) but numerous “en echelon” strike-slip features (Figures 4 and 5). The wedge grows by the accretion of thrust units
254 running parallel or subparallel to the backstop. Yet, the slope observed in the experiments by Martinez et al. (2002) and McClay
255 et al. (2004) is higher than the one we obtained (around 17° and 10° , respectively). This can be due to our lower basal friction
256 obtained using the carbon-kevlar film (Martinez et al., 2002; Konstantinovskaia and Malavieille, 2005), but this is also certainly

257 related to the erosive processes that maintain a lower slope angle and prevent the slope failure processes observed by McClay
258 et al. (2004). In addition, the transport and deposition of sediments during the experiment allows the formation of sedimentary
259 features that cannot be observed in experiments without erosion, such as large alluvial fans, which will ultimately be advected
260 into the wedge as piggy-back basins (Figures 4 and 8).

261 The angle of convergence influences the amount of slip partitioning, and thus the mode of deformation and the rate of wedge
262 growth (Chemenda et al., 2000). With a lower convergence angle, more time will be required to form an equivalent relief because
263 the shortening component of deformation will be reduced. This motivated our choice to use a convergence angle higher than
264 what is observed in the Southern Alps (30° and 11° , respectively). It also controls the capacity of drainage networks to develop
265 as the wedge grows. A minimum slope and length is required for a stream to maintain, as shown on Figures 4 and 5. In our
266 experiment, the first streams draining from the divide to the front of the wedge appear for a prowedge around 20 cm long and
267 for a slope of $\sim 15^\circ$. Therefore, it is likely that perennial rivers will not form if the convergence angle is too low and the minimal
268 angle has to be tested in our experimental setup. At low angle, a mountain range-like topography forms but is very narrow
269 (McClay et al., 2004; Leever et al., 2011) which is not suitable for a drainage network to develop. Based on previous works in
270 oblique collision but without erosion, a minimal angle of a dozen of degree might be required (McClay et al., 2004; Leever et al.,
271 2011).

272 The backstop geometry is not expected to affect the degree of partitioning of the motion (Martinez et al., 2002). However, it
273 can modify the localization of deformation and thus, its distribution across the wedge. Using a ramp rather than a simple point
274 as a velocity discontinuity favors the localization of deformation right above the discontinuity and prevents the development
275 of multiple retro-shear structures (Martinez et al., 2002; McClay et al., 2004; Leever et al., 2011). It might also favor a quite
276 homogeneous velocity field at the surface of the wedge (Martinez et al., 2002). Finally, the geometry of the ramp can affect the
277 position of the divide (Cruz et al., 2008). It is thus manifest that the capacity of the tectonic system to distribute deformation
278 depends directly on its geometry, and therefore care must be taken in extending our results to other configurations.

279 *4.2. Relation with previous works*

280 Our study corroborates the results of Castellort et al. (2012) showing that the rivers of the Southern Alps of New Zealand
281 are deformed in response to a distributed shear across the relief. However, the geometry of the systems is not equivalent, leading
282 to some important differences in the final morphology of the wedge and associated drainage system geometry.

283 The numerical setup in Castellort et al. (2012) is very different from our, as it consists of a mature and symmetrical drainage
284 entering an area of shear deformation. In this configuration, rivers experience increasing deformation as they are advected

285 south-westward and a clear EW gradient of the river orientation can be observed (Figure 1b). In our experiment, rivers develop
286 and deform simultaneously over the entire length of the orogenic wedge, such that there is no lateral gradient of deformation.
287 In addition, we used a convergence angle of 30° , when it is only of 11° in the numerical models and in the Southern Alps. This
288 higher angle increases the compressive component, which is equal to 40% of the fault-parallel component in our experiment and
289 to only 20% in numerical models and in the Southern Alps. In addition, a larger fraction of this component is distributed across
290 the experimental wedge ($\sim 50\%$ vs $\sim 34\%$). However, in the three settings, $\sim 30\%$ of the motion parallel to the main fault is
291 distributed across the relief.

292 The distribution of motion across the relief is also an important difference between our experiment and the work of Castelltort
293 et al. (2012). In their study, both components of the velocity are imposed to decrease linearly from the southern to the northern
294 edge of the model, whereas the velocity pattern that emerges in our experiments is less controlled and more variable since it
295 is influenced by the structural evolution of the wedge (Figures 10 and 11). This is in better agreement with the natural case,
296 as GPS data in the Southern Alps show that the orientation of the velocity vectors is not constant from the South-East to the
297 North-West side of the range (Beavan and Haines, 2001). In addition, the ratio between the two components of the motion
298 also evolves across the range, but contrary to what we observed, the fault-parallel component decreases faster than the fault-
299 perpendicular one (Beavan and Haines, 2001). It is beyond the scope of this study to discuss the influence of such differences in
300 the final morphology of the rivers. It is likely that it will modify the amount of deformation recorded by rivers but it should not
301 prevent rivers from recording deformation.

302 Finally, in each case, materials exhibit a Coulomb-like mechanical behavior and erosion is primarily limited to fluvial processes.
303 However, the exact mechanisms and rates of erosion, transport and deposition inevitably differ between numerical models,
304 laboratory experiments and natural settings (see Discussion in Graveleau et al., 2015). This can partly explain the larger valleys
305 and more irregular drainage basins in our laboratory experiments compared with numerical simulations of Castelltort et al.
306 (2012).

307 *4.3. Competition between the imposed rotation and the river dynamics*

308 Once the geometry of the experimental system is set, the shortening and the precipitation rates must be carefully chosen
309 because these first-order parameters strongly control the wedge morphology and the deformation mechanisms. They must also
310 be set so that passive deformation and river erosion can be expressed simultaneously in the landscape during the experiment.
311 The precipitation rate must be high enough to keep pace with the relief growth but low enough to let the drainage network evolve
312 in a steady state of equilibrium with tectonics. If precipitation rate is too high compared to shortening, it is very likely that

313 rivers will be reset permanently and will not record the imposed deformation. The shortening rate must be moderate as shown
314 by preliminary experiments indicating that high shortening rates induce such a rapid growth of the relief that gravitational
315 processes (landslides) become a dominant erosion process shaping the morphology of the whole wedge. If shortening is too low,
316 rivers do not deform and we expect a drainage network perpendicular to the main axis of the wedge independently of the initial
317 imposed obliquity. More experiments must be carried out to explore the range of parameters leading to these extreme cases.

318 The experiment presented in this paper was designed to document an intermediate situation, in which both fluvial erosion
319 and passive deformation are expressed in the landscape. The shortening rate was imposed by the experimental conditions
320 and the precipitation rate was tuned to ensure the development of a drainage network but of a sufficient (i.e., visible in the
321 landscape) deformation. As described above, rivers tend to rotate clockwise (Figure 8) and we interpret this rotation as a result
322 of distributed shear across the wedge, as suggested in New Zealand and in Lebanon (Castelltort et al., 2012; Goren et al., 2015).

323 Our experiment was recorded by pictures taken at high frequency (every 30 seconds) and it is therefore possible to document
324 accurately the evolution of a stream and its potential reorganization. Five channels were mapped on these pictures, their mean
325 orientation was determined visually (Figure 13a), and then compared to the theoretical evolution of an equivalent passive marker,
326 i.e., a marker that would appear at the same time, at the same position and with the same initial orientation (Figure 13b).
327 The average orientation of each channel increases with time, in agreement with the trend expected for a passive marker, but
328 the observed values differ from the theoretical one. Channels can be more clockwise-rotated than expected, or less rotated, and
329 sometimes they can match the model (Figure 13b), demonstrating that rivers in this experiment do not behave like simple passive
330 markers. It is difficult to propose a complete explanation of this behavior based on the present-day data set. It is probably
331 linked to the fact that the drainage network is highly dynamic, with substantial erosion, deposition and network reorganization,
332 and this fluvial activity can modify the average orientation of a stream.

333 5. Conclusions

334 We developed an experimental model of a doubly-vergent asymmetric wedge in oblique convergence setting including surface
335 processes (erosion, sediment transport and deposition). Based on the quantitative analysis of model surface kinematics and
336 drainage network geometric evolution, we show that in such tectonic context :

- 337 1. Model deformation is only partially accommodated on the main fault: $\sim 30\%$ of the backstop-parallel and $\sim 50\%$ of the
338 backstop-perpendicular components of shortening are diffusively distributed across the wedge.
- 339 2. The backstop-parallel component of shortening decreases regularly from the front of the wedge to the divide.

- 340 3. The backstop-perpendicular component of shortening is controlled by the main tectonics features i.e., by the former fronts
341 advected into the wedge. This component mainly exists in the frontal area of the wedge and decreases to almost zero
342 toward its inner part.
- 343 4. The total amount of shear does not change during the experiment but as the length of the pro-wedge increases though
344 time, it is distributed over an increasingly larger area.
- 345 5. This pattern imposes a rotation to any surface marker, that can be predicted from the velocity field.
- 346 6. Consequently, the drainage network rotates with respect to the main axis of the range. However, accurate monitoring of
347 channel evolution during the experiments documents their constant adjustment to deformation by erosional processes, and
348 thus highlight the dynamic nature of rivers as markers of deformation.

349 These results confirm that rivers can record a large amount of distributed horizontal deformation, as suggested in New
350 Zealand and in Lebanon (Castelltort et al., 2012; Goren et al., 2015). More experiments are however required to investigate
351 further how river dynamics competes with surface deformation. This will allow to improve the theoretical framework necessary
352 to interpret large-scale deformation of drainage networks in natural settings.

353 *Acknowledgements*

354 We are thankful to Patrice Rey and Karen Leever for their comments that strongly improve the quality of the paper. We
355 thank C. Romano for his strong support for the design of the setup and during the experiments. This work was supported by
356 the Swiss National Science Foundation project “Earth Surface Signaling Systems” (grant No 200021-146822).

357 **References**

- 358 Adams J. Contemporary uplift and erosion of the Southern Alps, New Zealand. Geological Society of America Bulletin 1980;91(1
359 Part II):1–114.
- 360 Allen C. Transcurrent faults in continental areas. Philosophical Transactions of the Royal Society of London A: Mathematical,
361 Physical and Engineering Sciences 1965;258(1088):82–9.
- 362 Attal M. Geomorphology: Rivers split as mountains grow. Nature Geoscience 2009;2(11):747–8.
- 363 Babault J, Van Den Driessche J, Teixell A. Longitudinal to transverse drainage network evolution in the High Atlas (Morocco):
364 The role of tectonics. Tectonics 2012;31(4).

365 Beavan J, Haines J. Contemporary horizontal velocity and strain rate fields of the Pacific-Australian plate boundary zone
366 through New Zealand. *Journal of Geophysical Research: Solid Earth* (1978–2012) 2001;106(B1):741–70.

367 Bishop P. Drainage rearrangement by river capture, beheading and diversion. *Progress in Physical Geography* 1995;19(4):449–73.

368 Bonnet S. Shrinking and splitting of drainage basins in orogenic landscapes from the migration of the main drainage divide.
369 *Nature Geoscience* 2009;2(11):766–771.

370 Braun J, Beaumont C. Three-dimensional numerical experiments of strain partitioning at oblique plate boundaries: Implications
371 for contrasting tectonic styles in the southern Coast Ranges, California, and central South Island, New Zealand. *Journal of*
372 *Geophysical Research: Solid Earth* 1995;100(B9):18059–74.

373 Brocard G, Van Der Beek P, Bourlès D, Siame L, Mugnier JL. Long-term fluvial incision rates and postglacial river relaxation
374 time in the French Western Alps from 10 Be dating of alluvial terraces with assessment of inheritance, soil development and
375 wind ablation effects. *Earth and Planetary Science Letters* 2003;209(1):197–214.

376 Brocard G, Willenbring J, Suski B, Audra P, Authemayou C, Cosenza-Murales B, Morán-Ical S, Demory F, Rochette P,
377 Vennemann T, Holliger K, Teyssier C. Rate and processes of river network rearrangement during incipient faulting: The case
378 of the Cahabón River, Guatemala. *American Journal of Science* 2012;312(5):449–507.

379 Brookfield M. The evolution of the great river systems of southern Asia during the Cenozoic India-Asia collision: rivers draining
380 southwards. *Geomorphology* 1998;22(3):285–312.

381 Burbidge DR, Braun J. Analogue models of obliquely convergent continental plate boundaries. *Journal of Geophysical Research:*
382 *Solid Earth* 1998;103(B7):15221–37.

383 Castelltort S, Goren L, Willett SD, Champagnac JD, Herman F, Braun J. River drainage patterns in the New Zealand Alps
384 primarily controlled by plate tectonic strain. *Nature Geoscience* 2012;5(10):744–8.

385 Castelltort S, Simpson G. River spacing and drainage network growth in widening mountain ranges. *Basin Research*
386 2006;18(3):267–76.

387 Chemenda A, Lallemand S, Bokun A. Strain partitioning and interplate friction in oblique subduction zones: constraints provided
388 by experimental modeling. *Journal of Geophysical Research: Solid Earth* 2000;105(B3):5567–81.

389 Chen CW, Zebker HA. Phase unwrapping for large sar interferograms: statistical segmentation and generalized network models.
390 *Geoscience and Remote Sensing, IEEE Transactions on* 2002;40(8):1709–19.

391 Clark M, Schoenbohm L, Royden L, Whipple K, Burchfiel B, Zhang X, Tang W, Wang E, Chen L. Surface uplift, tectonics, and
392 erosion of eastern Tibet from large-scale drainage patterns. *Tectonics* 2004;23(1):TC1006.

393 Cox SC, Sutherland R. Regional geological framework of South Island, New Zealand, and its significance for understanding the
394 active plate boundary. *A continental plate boundary: tectonics at South Island, New Zealand* 2007;:19–46.

395 Cruz L, Teyssier C, Perg L, Take A, Fayon A. Deformation, exhumation, and topography of experimental doubly-vergent orogenic
396 wedges subjected to asymmetric erosion. *Journal of Structural Geology* 2008;30(1):98–115.

397 Davis D, Suppe J, Dahlen F. Mechanics of fold-and-thrust belts and accretionary wedges. *Journal of Geophysical Research*
398 1983;88(B2):1153–72.

399 Dominguez S, Lallemand S, Malavieille J, Schnürle P. Oblique subduction of the Gagua Ridge beneath the Ryukyu accretionary
400 wedge system: Insights from marine observations and sandbox experiments. *Marine Geophysical Researches* 1998;20(5):383–
401 402.

402 Ferrater M, Booth-Rea G, Pérez-Peña JV, Azañón JM, Giaconia F, Masana E. From extension to transpression: Quater-
403 nary reorganization of an extensional-related drainage network by the Alhama de Murcia strike-slip fault (eastern Betics).
404 *Tectonophysics* 2015;.

405 Giachetta E, Refice A, Capolongo D, Gasparini NM, Pazzaglia FJ. Orogen-scale drainage network evolution and response to
406 erodibility changes: insights from numerical experiments. *Earth Surface Processes and Landforms* 2014;39(9):1259–68.

407 Goren L, Castelltort S, Klinger Y. Modes and rates of horizontal deformation from rotated river basins: Application to the Dead
408 Sea fault system in Lebanon. *Geology* 2015;43(9):843–6.

409 Graveleau F, Dominguez S. Analogue modelling of the interaction between tectonics, erosion and sedimentation in foreland
410 thrust belts. *Comptes Rendus Geoscience* 2008;340(5):324–33.

411 Graveleau F, Hurtrez JE, Dominguez S, Malavieille J. A new experimental material for modeling relief dynamics and interactions
412 between tectonics and surface processes. *Tectonophysics* 2011;513(1):68–87.

413 Graveleau F, Strak V, Dominguez S, Malavieille J, Chatton M, Manighetti I, Petit C. Experimental modelling of tectonics–
414 erosion–sedimentation interactions in compressional, extensional, and strike–slip settings. *Geomorphology* 2015;244:146–68.

415 Griffiths GA, McSaveney M. Distribution of mean annual precipitation across some stepland regions of New Zealand. *New
416 Zealand journal of science* 1983;26(2):197–209.

417 Gutscher MA, Kukowski N, Malavieille J, Lallemand S. Cyclical behavior of thrust wedges: Insights from high basal friction
418 sandbox experiments. *Geology* 1996;24(2):135–8.

419 Hallet B, Molnar P. Distorted drainage basins as markers of crustal strain east of the Himalaya. *Journal of Geophysical Research:*
420 *Solid Earth* 2001;106(B7):13697–709.

421 Herman F, Cox SC, Kamp PJ. Low-temperature thermochronology and thermokinematic modeling of deformation, exhumation,
422 and development of topography in the central Southern Alps, New Zealand. *Tectonics* 2009;28(5).

423 Hicks DM, Hill J, Shankar U. Variation of suspended sediment yields around New Zealand: the relative importance of rainfall
424 and geology. *IAHS publication* 1996;:149–56.

425 Hollingsworth J, Jackson J, Walker R, Nazari H. Extrusion tectonics and subduction in the eastern South Caspian region since
426 10 Ma. *Geology* 2008;36(10):763–6.

427 Hovius N. Regular spacing of drainage outlets from linear mountain belts. *Basin Research* 1996;8:29–44.

428 Hubert-Ferrari A, Armijo R, King G, Meyer B, Barka A. Morphology, displacement, and slip rates along the North Anatolian
429 Fault, Turkey. *Journal of Geophysical Research: Solid Earth* 2002;107(B10):ETG–9.

430 Hubert-Ferrari A, King G, van der Woerd J, Villa I, Altunel E, Armijo R. Long-term evolution of the North Anatolian Fault:
431 new constraints from its eastern termination. *Geological Society, London, Special Publications* 2009;311(1):133–54.

432 Kirby E. Geomorphology: Tectonically twisted rivers. *Nature Geoscience* 2012;5(10):688–9.

433 Klinger Y, Etchebes M, Tapponnier P, Narteau C. Characteristic slip for five great earthquakes along the Fuyun fault in China.
434 *Nature Geoscience* 2011;4(6):389–92.

435 Konstantinovskaia E, Malavieille J. Erosion and exhumation in accretionary orogens: Experimental and geological approaches.
436 *Geochemistry, Geophysics, Geosystems* 2005;6(2).

437 Koons PO. Three-dimensional critical wedges: Tectonics and topography in oblique collisional orogens. *Journal of Geophysical*
438 *Research: Solid Earth* 1994;99(B6):12301–15.

439 Krystek M, Anton M. A least-squares algorithm for fitting data points with mutually correlated coordinates to a straight line.
440 *Measurement Science and Technology* 2011;22(3):035101.

441 Lavé J. Landscape inversion by stream piracy. *Nature* 2015;520(7548):442–4.

- 442 Leever KA, Gabrielsen RH, Sokoutis D, Willingshofer E. The effect of convergence angle on the kinematic evolution of strain par-
443 titioning in transpressional brittle wedges: Insight from analog modeling and high-resolution digital image analysis. *Tectonics*
444 2011;30(2).
- 445 Li H, Van der Woerd J, Sun Z, Si J, Tapponnier P, Pan J, Liu D, Chevalier ML. Co-seismic and cumulative offsets of the recent
446 earthquakes along the Karakax left-lateral strike-slip fault in western Tibet. *Gondwana Research* 2012;21(1):64–87.
- 447 Malavieille J. Modelisation experimentale des chevauchements imbriques; application aux chaines de montagnes. *Bulletin de la*
448 *Société géologique de France* 1984;1:129–38.
- 449 Martinez A, Malavieille J, Lallemand S, Collot JY. Partition de la déformation dans un prisme d'accrétion sédimentaire en
450 convergence oblique: approche expérimentale. *Bulletin de la Societe Geologique de France* 2002;173(1):17–24.
- 451 McClay K, Whitehouse P, Dooley T, Richards M. 3d evolution of fold and thrust belts formed by oblique convergence. *Marine*
452 *and Petroleum Geology* 2004;21(7):857–77.
- 453 Molnar P, Anderson HJ, Audoine E, Eberhart-Phillips D, Gledhill KR, Klosko ER, McEvelly TV, Okaya D, Savage MK,
454 Stern T, Wu F. Continuous deformation versus faulting through the continental lithosphere of New Zealand. *Science*
455 1999;286(5439):516–9.
- 456 Norris RJ, Cooper AF. Late Quaternary slip rates and slip partitioning on the Alpine Fault, New Zealand. *Journal of Structural*
457 *Geology* 2001;23(2):507–20.
- 458 Norris RJ, Toy VG. Continental transforms: A view from the Alpine Fault. *Journal of Structural Geology* 2014;64:3–31.
- 459 Perron JT, Dietrich WE, Kirchner JW. Controls on the spacing of first-order valleys. *Journal of Geophysical Research: Earth*
460 *Surface* 2008;113(F4).
- 461 Ramsey LA, Walker RT, Jackson J. Geomorphic constraints on the active tectonics of southern taiwan. *Geophysical Journal*
462 *International* 2007;170(3):1357–72.
- 463 Replumaz A, Lacassin R, Tapponnier P, Leloup P. Large river offsets and Plio-Quaternary dextral slip rate on the Red River
464 fault (Yunnan, China). *Journal of Geophysical Research: Solid Earth* 2001;106(B1):819–36.
- 465 Roe GH, Montgomery DR, Hallet B. Orographic precipitation and the relief of mountain ranges. *Journal of Geophysical Research:*
466 *Solid Earth* 2003;108(B6).

467 Santimano T, Rosenau M, Oncken O. Intrinsic versus extrinsic variability of analogue sand-box experiments—Insights from
468 statistical analysis of repeated accretionary sand wedge experiments. *Journal of Structural Geology* 2015;75:80–100.

469 Sutherland R. Cenozoic bending of New Zealand basement terranes and Alpine Fault displacement: a brief review. *New Zealand*
470 *Journal of Geology and Geophysics* 1999;42(2):295–301.

471 Tucker GE, Slingerland R. Drainage basin responses to climate change. *Water Resources Research* 1997;33(8):2031–47.

472 Upton P, Koons PO, Eberhart-Phillips D. Extension and partitioning in an oblique subduction zone, New Zealand: Constraints
473 from three-dimensional numerical modeling. *Tectonics* 2003;22(6).

474 Walcott R. Modes of oblique compression: Late Cenozoic tectonics of the South Island of New Zealand. *Reviews of Geophysics*
475 1998;36(1):1–26.

476 Walker R, Jackson J. Offset and evolution of the Gowk fault, SE Iran: a major intra-continental strike-slip system. *Journal of*
477 *structural Geology* 2002;24(11):1677–98.

478 Wallace LM, Beavan J, McCaffrey R, Berryman K, Denys P. Balancing the plate motion budget in the South Island, New
479 Zealand using GPS, geological and seismological data. *Geophysical Journal International* 2007;168(1):332–52.

480 Willett S, Beaumont C, Fullsack P. Mechanical model for the tectonics of doubly vergent compressional orogens. *Geology*
481 1993;21(4):371–4.

482 Willett SD, McCoy SW, Perron JT, Goren L, Chen CY. Dynamic reorganization of river basins. *Science* 2014;343(6175):1248765.

483 Yang R, Fellin MG, Herman F, Willett SD, Wang W, Maden C. Spatial and temporal pattern of erosion in the Three Rivers
484 Region, southeastern Tibet. *Earth and Planetary Science Letters* 2016;433:10–20.

485 Yang R, Willett SD, Goren L. In situ low-relief landscape formation as a result of river network disruption. *Nature*
486 2015;520(7548):526–9.

Model thickness	6 cm
Precipitations	0 to 50 mm/h
Imposed motion	7.5 cm/h
Convergence angle	30 °
Backstop dip	60 °
Total shortening	75 cm

Table 1: Main characteristics and boundary conditions of the experiment.

	Glass beads	PVC	Silica Powder	Talcum	Kaolinite	Water	C	μ
MatIV	37%	19%	24%	-	-	20%	750 Pa	1.13
MTK	34%	18%	-	22%	1%	25%	280 Pa	0.46

Table 2: Composition and characteristics of the two analogue materials used in the model (this study, Graveleau and Dominguez, 2008, and Graveleau et al., 2011). C is the cohesion and μ the coefficient of internal friction.

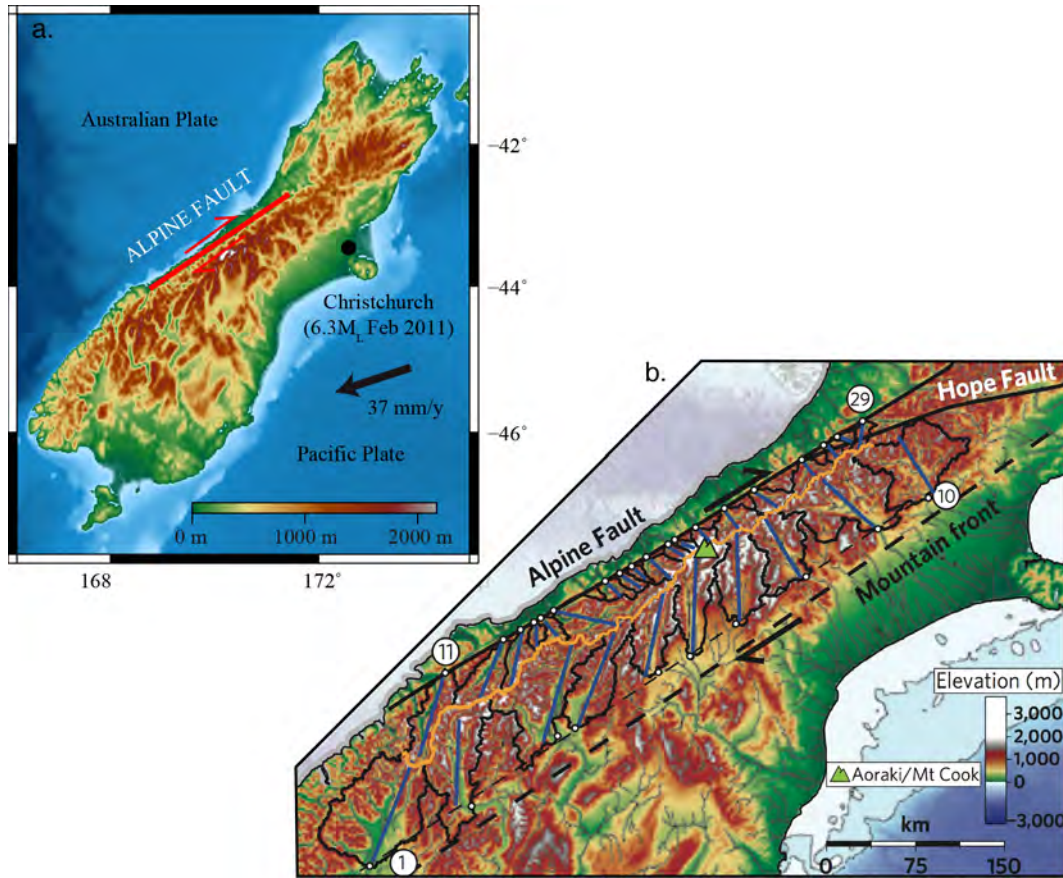


Figure 1: a) Simplified geodynamic context of the South Island of New Zealand. b) Topography of the South Island with major river basins (black), main river orientation (blue) and the main divide (orange) (modified from Castelltort et al., 2012).

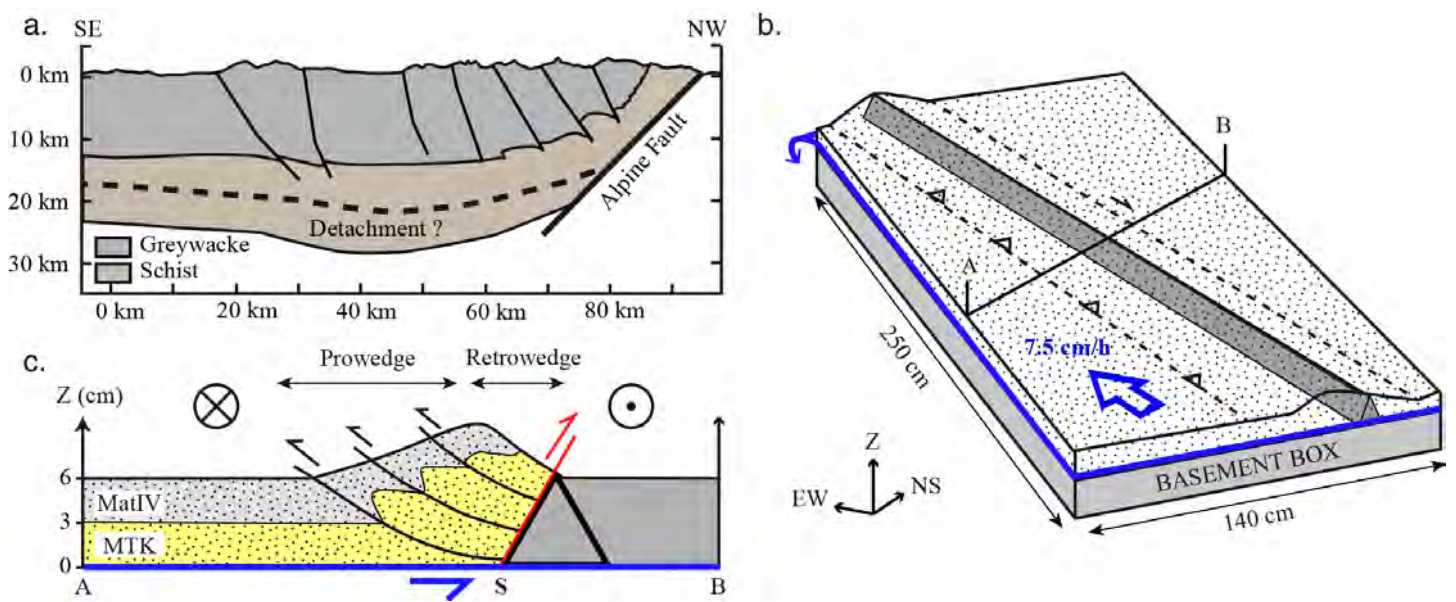


Figure 2: a) Simplified cross-section of the Southern Alps of New Zealand (modified from Herman et al., 2009). Experimental setup in b) side view and c) cross-section (see text for details about the materials). S indicates the velocity discontinuity.

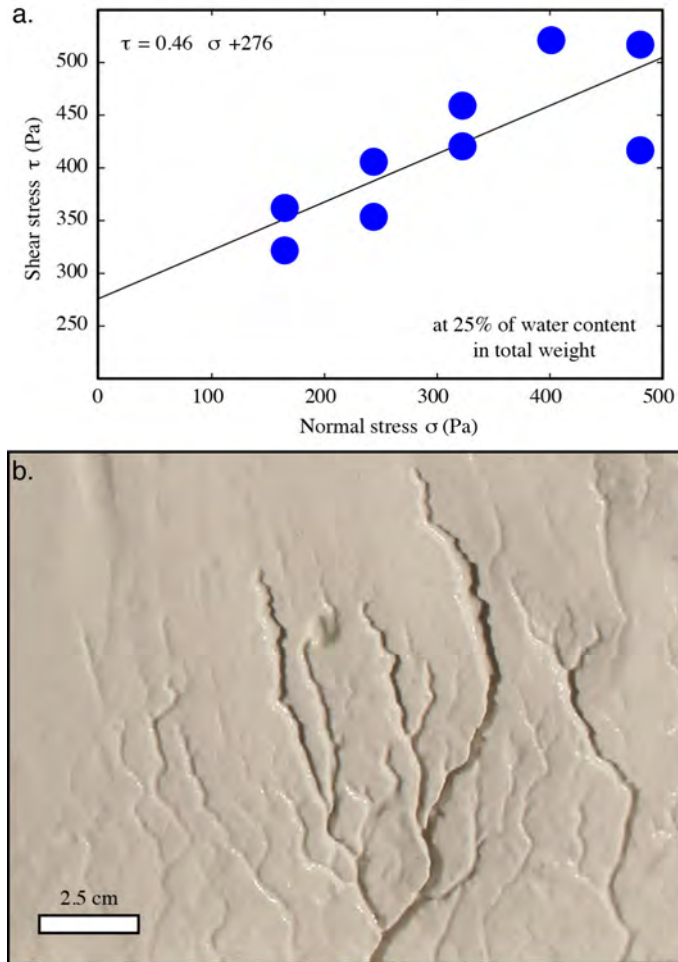


Figure 3: Properties of the analogue material used for the lower layer of the model (the MTK). a) Mohr-Coulomb failure envelop for the MTK. The best-fit slope and the intercept with y-axis define the coefficient of internal friction and the cohesion, respectively. b) Drainage network in MTK after 70 minutes of rain, for a slope of 20° .

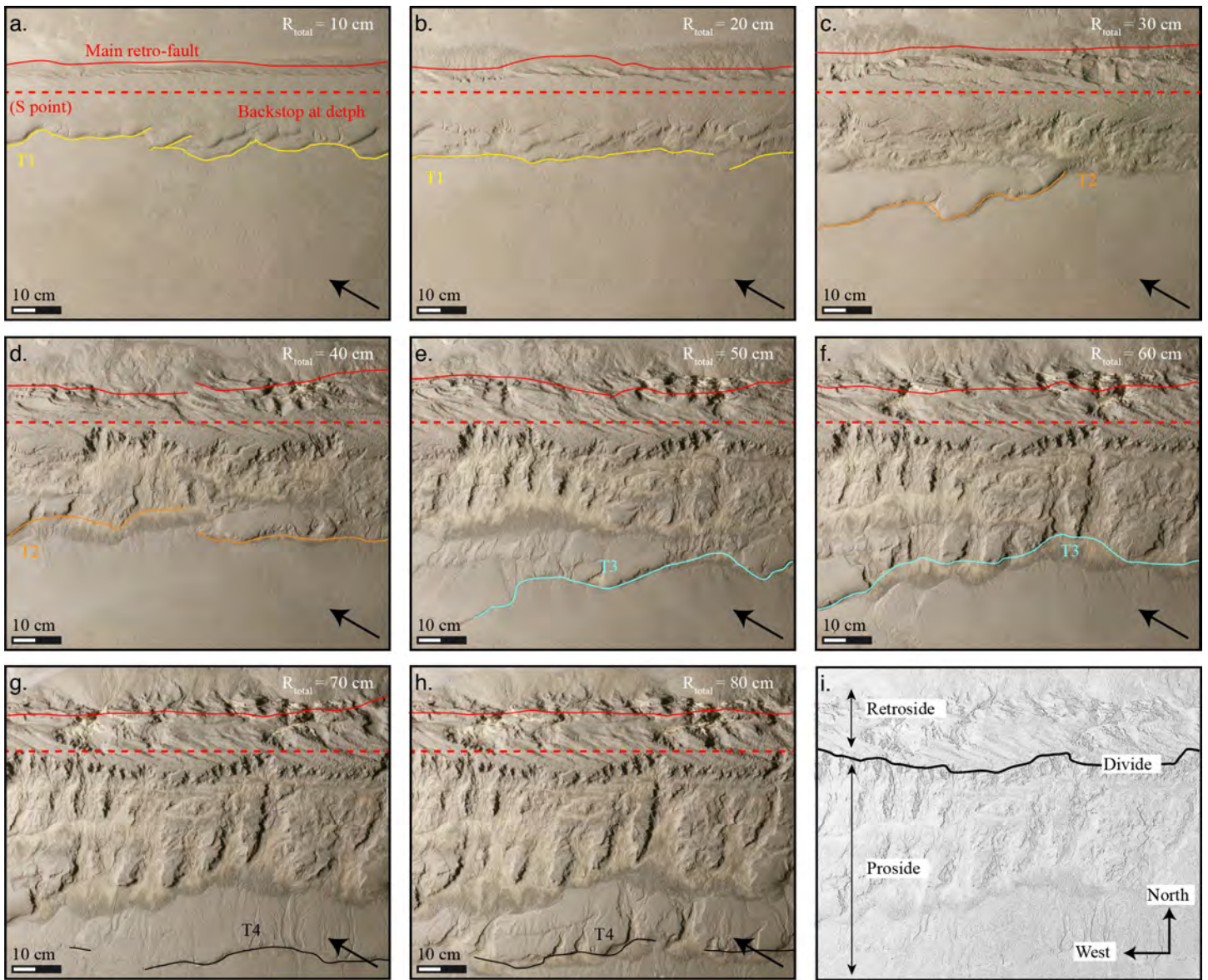


Figure 4: a-h) Evolution of the experimental wedge through time. Each picture corresponds to a shortening increment of ~ 10 cm. The main thrusts are labelled as they appear, from the first thrust (T1, in yellow) to the last one (T4, in black). The red dotted line indicates the position of the backstop at depth, i.e., of the velocity discontinuity (S point), the red line of the main retro-fault at the surface, the black arrow the direction of shortening. i) Definition of the divide (black line), pro- and retro-sides and spatial orientation.

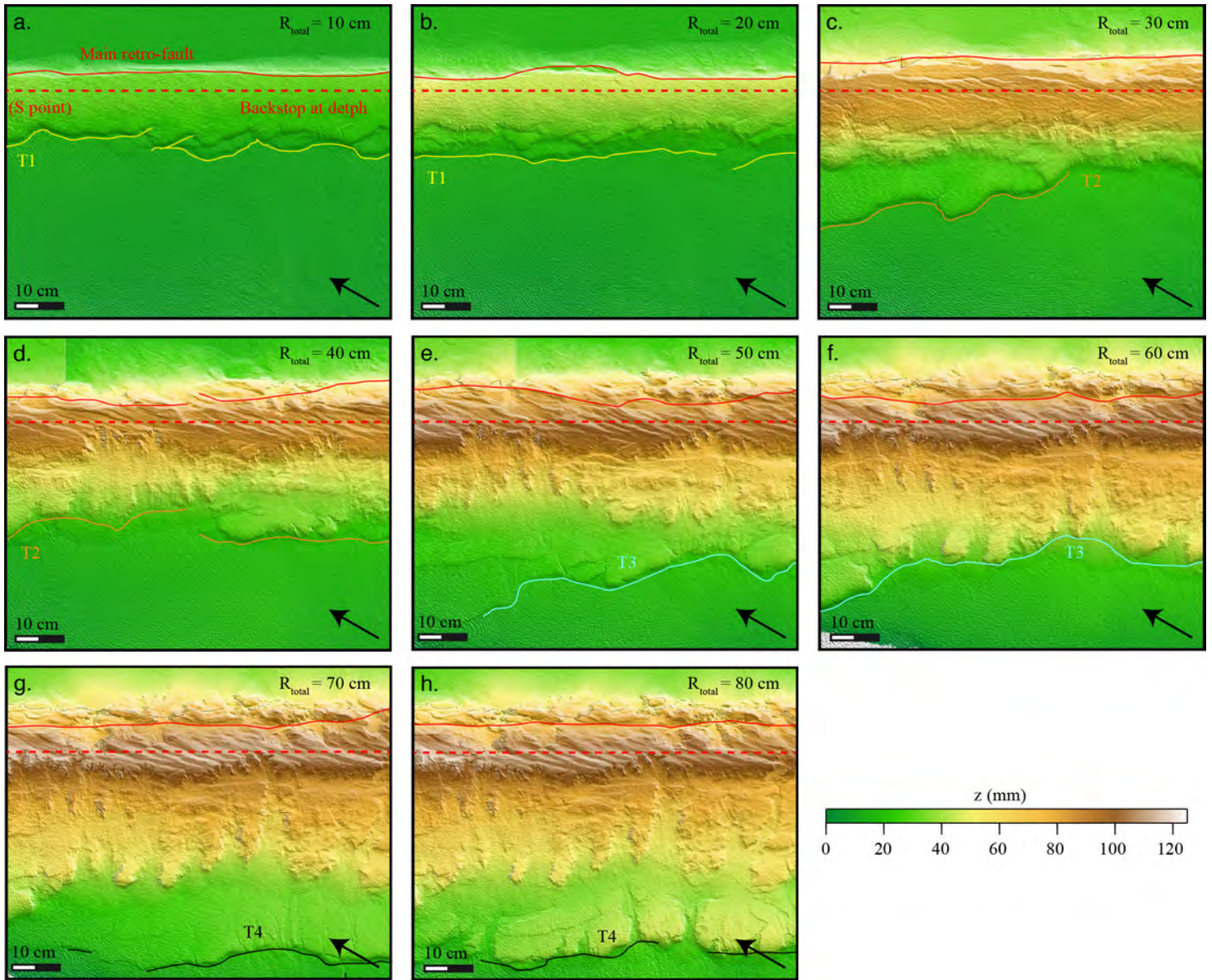


Figure 5: Evolution of the wedge morphology through time. Each DEM corresponds to a shortening increment of ~ 10 cm and is associated to the equivalent label (a–h) of Figure 4. The main thrusts are labelled as they appear, from the first thrust (T1, in yellow) to the last one (T4, in black). The red dotted line indicates the position of the backstop at depth, i.e., of the velocity discontinuity (S point), the red line of the main retro-fault at the surface, the black arrow the direction of shortening.

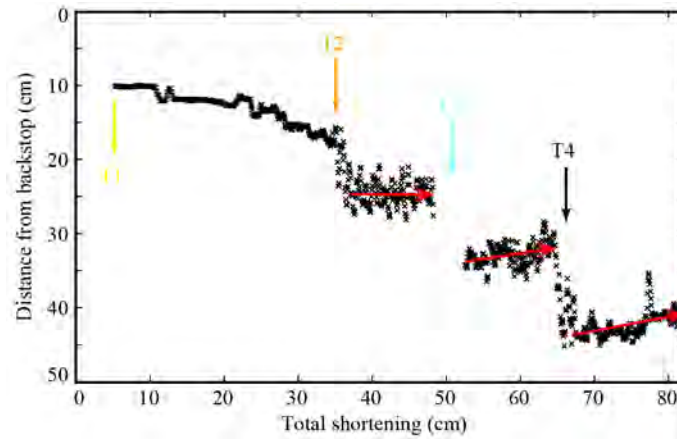


Figure 6: Average position of the wedge front through time (black crosses). The local front position is defined as the position of the main local velocity gradient and is then averaged in space, resulting in one average position for each picture. The emergence of the main thrusts (T1 to T4) are indicated, and the red arrows highlight the main trend. Distance is given from the position of the backstop at depth (S point).

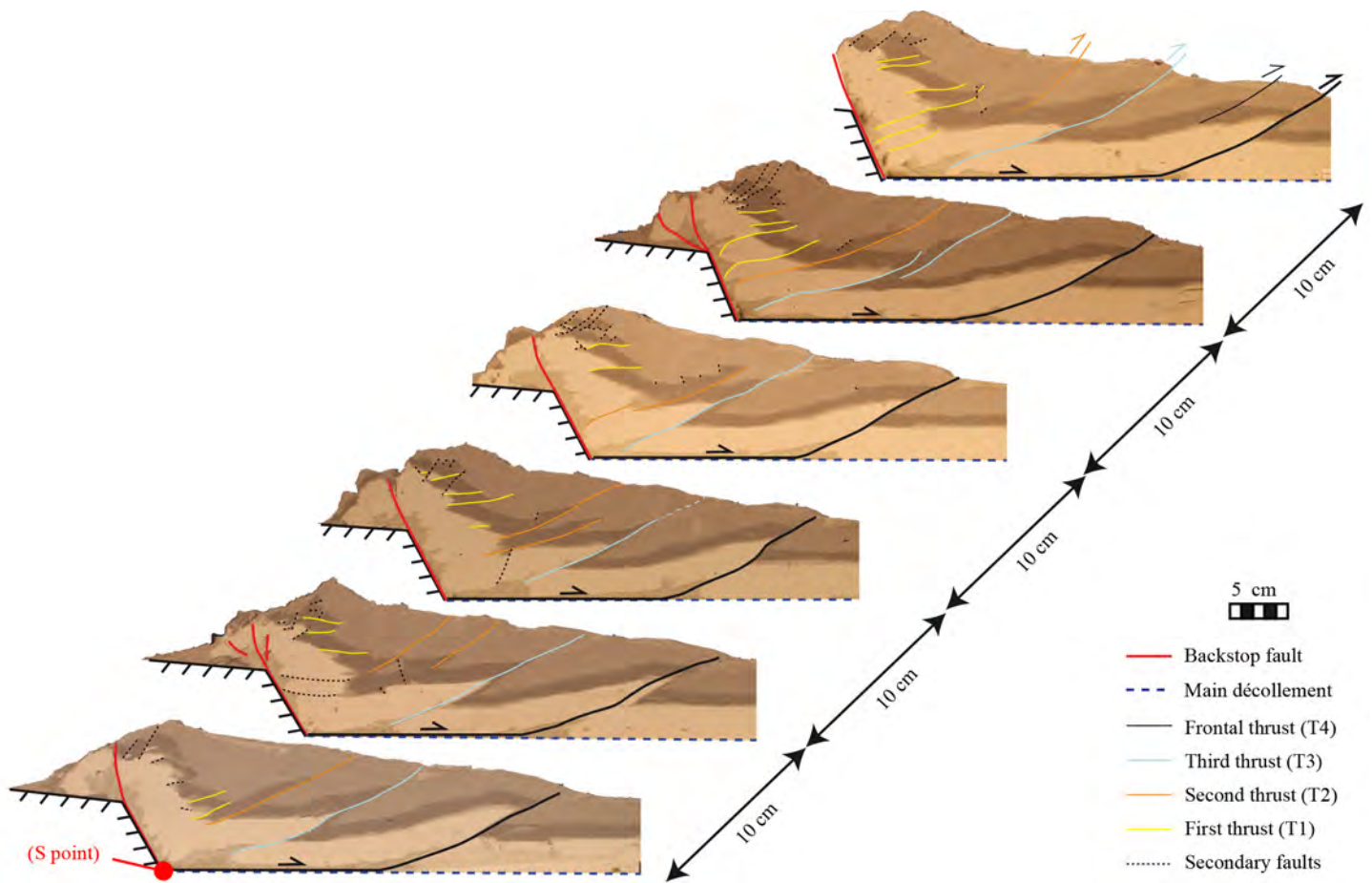


Figure 7: Cross-sections along the wedge at the end of the experiment. The main faults are mapped and are associated with the successive thrust T1 (yellow), T2 (orange), T3 (blue) and T4 (black). Small and secondary faults are also indicated (black dotted lines).

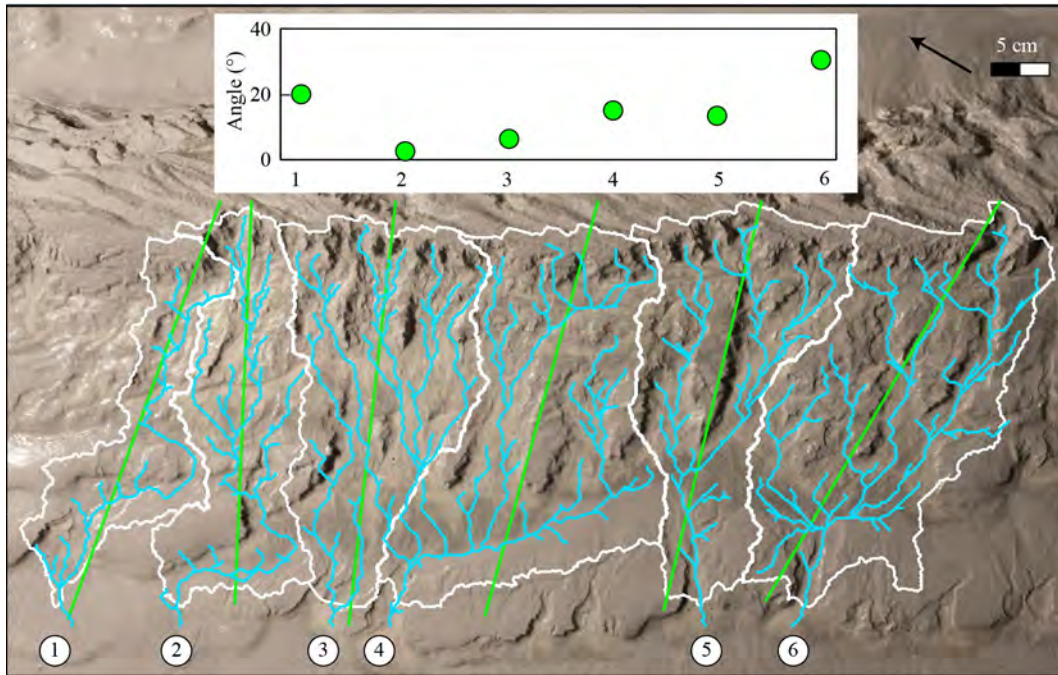


Figure 8: Orientation (green lines) of the main rivers (blue lines) after ~ 80 cm of shortening. White lines define the drainage basins and the black arrow indicates the direction of shortening.

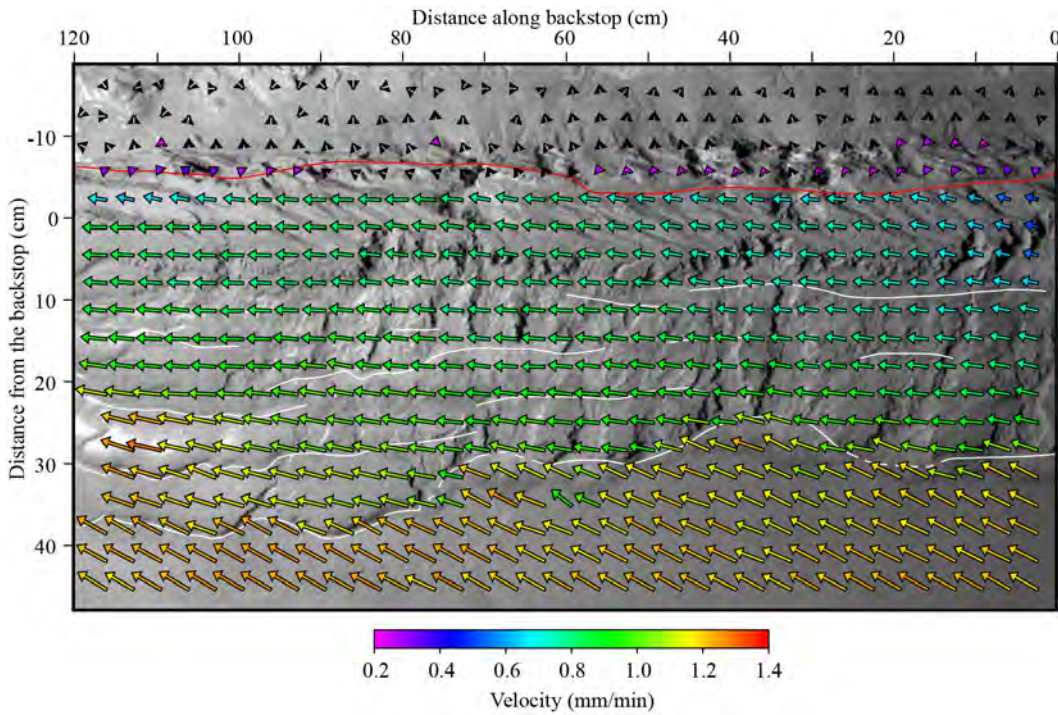


Figure 9: Typical velocity field map from image correlation between two pictures. The pro-shears are indicated in white and the main retro-shear in red.

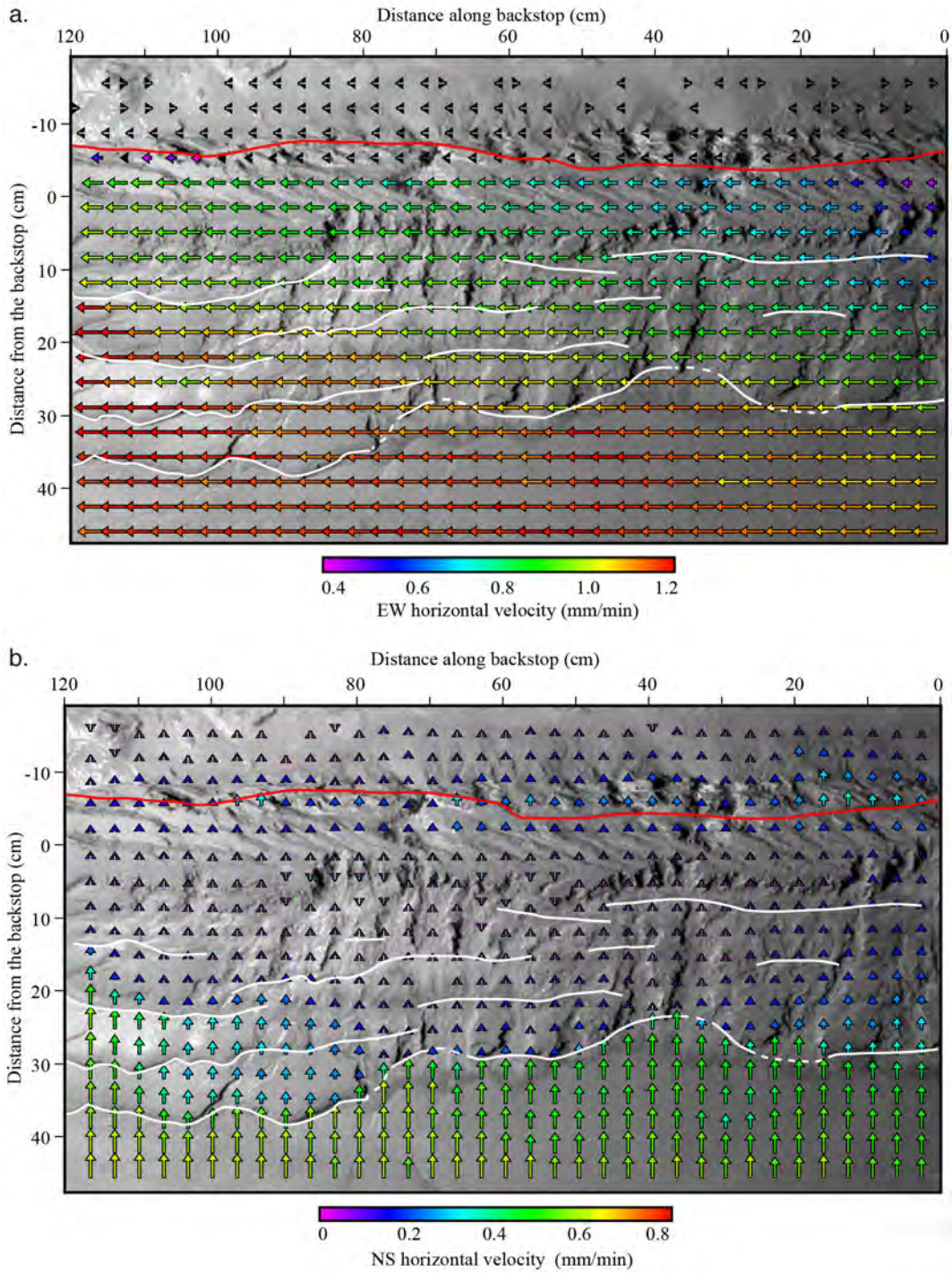


Figure 10: a) Fault-parallel (EW) and b) fault-perpendicular (NS) velocity field between two pictures. The pro-shears are indicated in white and the main retro-shear in red.

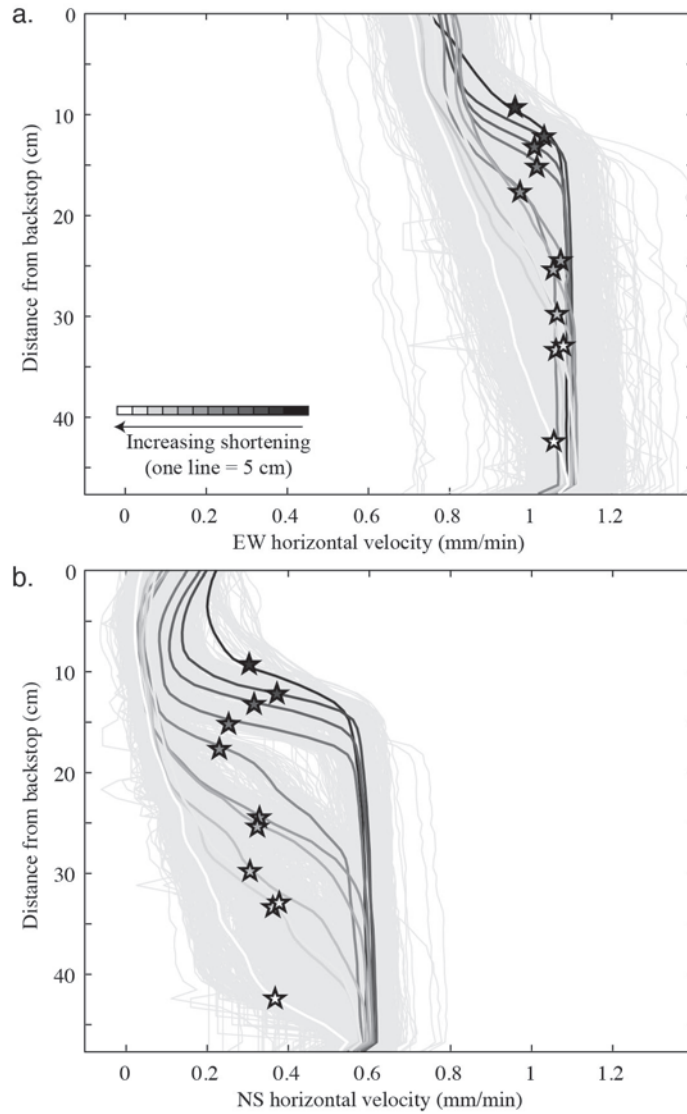


Figure 11: Average a) fault-parallel (EW) and b) fault-perpendicular (NS) velocity components across the wedge and in time. Light gray lines correspond to the velocity field for each picture, bold lines correspond to the average velocity field over 5 cm of shortening on which the average position of the wedge front during the corresponding time is indicated by a star. Distance is given from the position of the backstop at depth (S point).

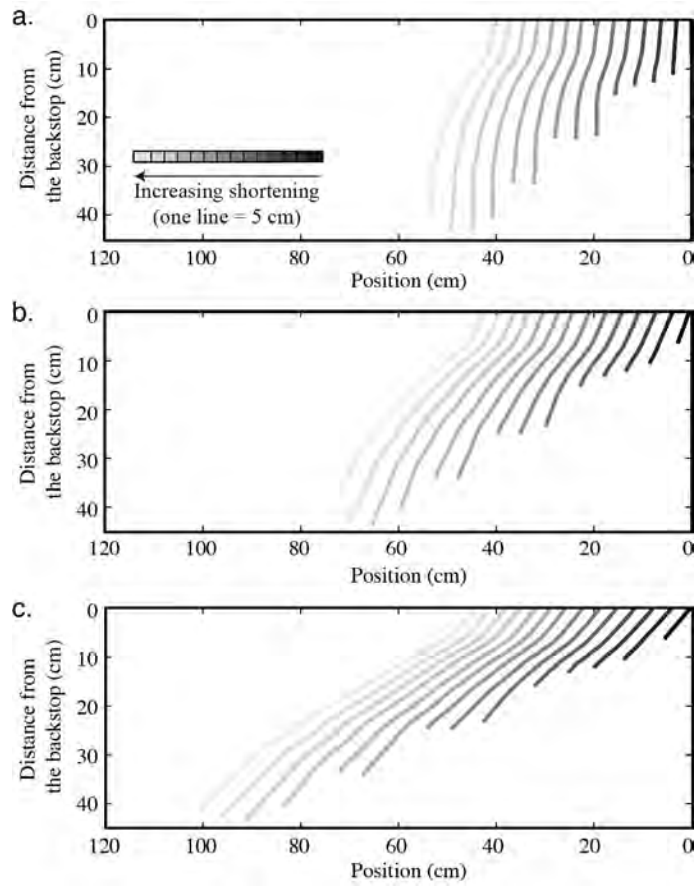


Figure 12: Rotation of a virtual passive marker due to imposed displacement during the whole duration of the experiment, with an initial orientation of a) 0° , b) 20° and c) 40° with respect to the North. Each line corresponds to an increment of 5 cm of total shortening. At each step, the length of the virtual marker is extended to the wedge front with the same initial orientation.

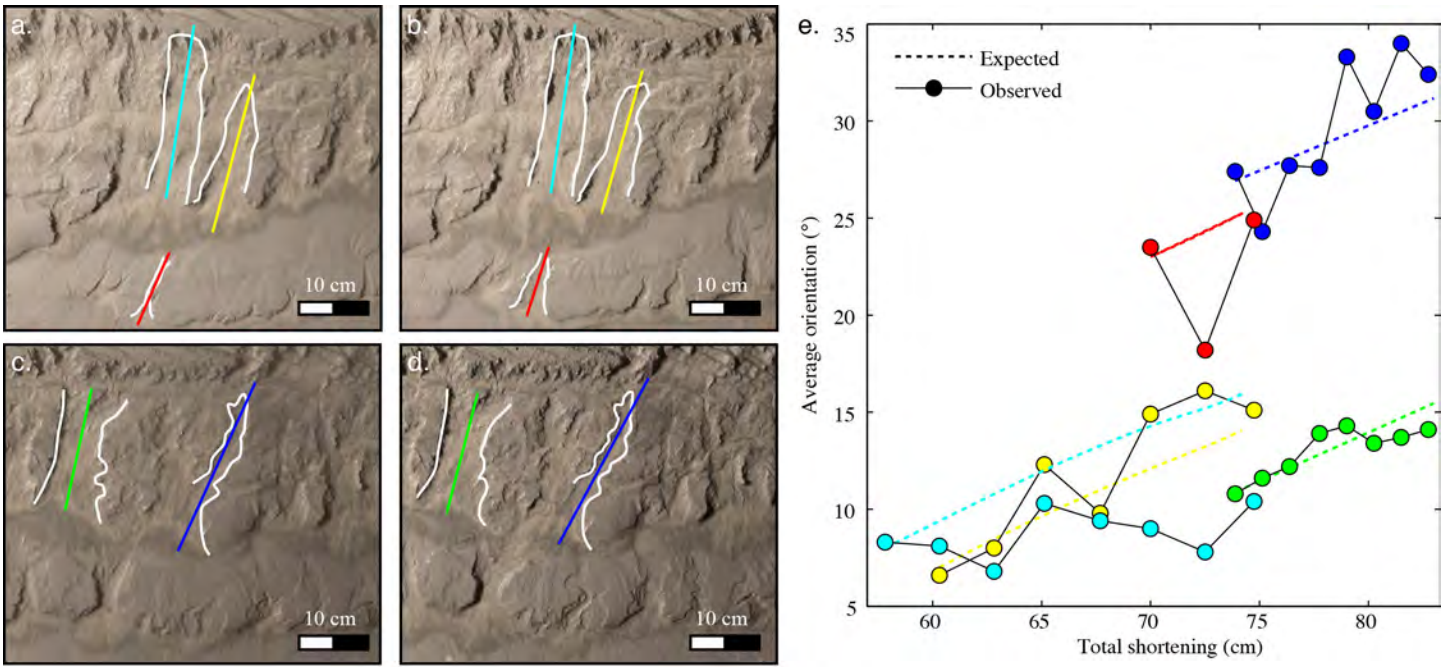


Figure 13: Examples of visually-defined orientation of a–b) three channels at 70 cm and 72.5 cm of shortening, respectively, and c–d) two channels at 75 and 77.5 cm of shortening, respectively. e) Average orientation with respect to the North of these five channels (circles) with respect to shortening, compared to the evolution expected for a virtual passive marker which would appear at the same moment, at the same position on the wedge surface and with the same initial orientation (dotted lines).